CHAPTER III

RESULTS AND DISCUSSIONS

3.1 Synthesis of $La_{0.7}Sr_{0.3}Fe_{1-x}M_xO_3$ (M= Cu, Ni, Al and Mn) (x= 0.1-0.4) by modified citrate method

The perovskite oxides were prepared by modified citrate method. The metal nitrates were dissolved in distilled water, which then reacted with the mole ratio of metal nitrate to citric acid, 1:2 to form metal-citrate-nitrate complexes. These metal-citrate complexes can undergo polymerization when ammonia solution was added. While, $NH_3 \cdot H_2O$ was added, the white fume of NH_4NO_3 was suddenly observed, which came from the free NO_3^- reacting with $NH_3 \cdot H_2O$ and generated heat. Then, the solution changed from clear red brown to clear deep brown solution (pH $\approx$ 9). The excess solvent was evaporated until a sticky gel was obtained. Finally, at around 200°C the spontaneous combustion occurred and the complex mixture changed the black oxide powder. The mixture powder was calcined at 900–1,000°C for 6 hours to achieve pure phase and remove residual organic compound. The calcined powder was ground and pressed to make a disc. Then the high density discs were obtained from sintering in air at 1,100–1,300°C for 10–15 hours, depending on the composition.

The effect of calcination process is in general favorable, predictable and related to the improvement of crystallite structure of as-synthesized powders. This process also removed residual water and other impurities. In case of sintering process, the effect of heat treatment is related to the substantial changes in all powder microstructures.

3.2 Characterization of the synthesized compounds

The structures of synthesized perovskite compounds were characterized by XRD and the surface morphology of the sintered discs were examined by SEM.

3.2.1 X-ray diffraction (XRD)

XRD was used to indicate the formation of the perovskite-type phase. The phase formations of perovskites were characterized after calcination and sintering. The diffraction peaks of perovskites were observed within the range of 20 to 70°.

3.2.1.1 Phase formation of $La_{0.7}Sr_{0.3}FeO_3$

The $La_{0.7}Sr_{0.3}FeO_3$ calcined powder was characterized by XRD and XRD pattern was illustrated in Figure 3.1.

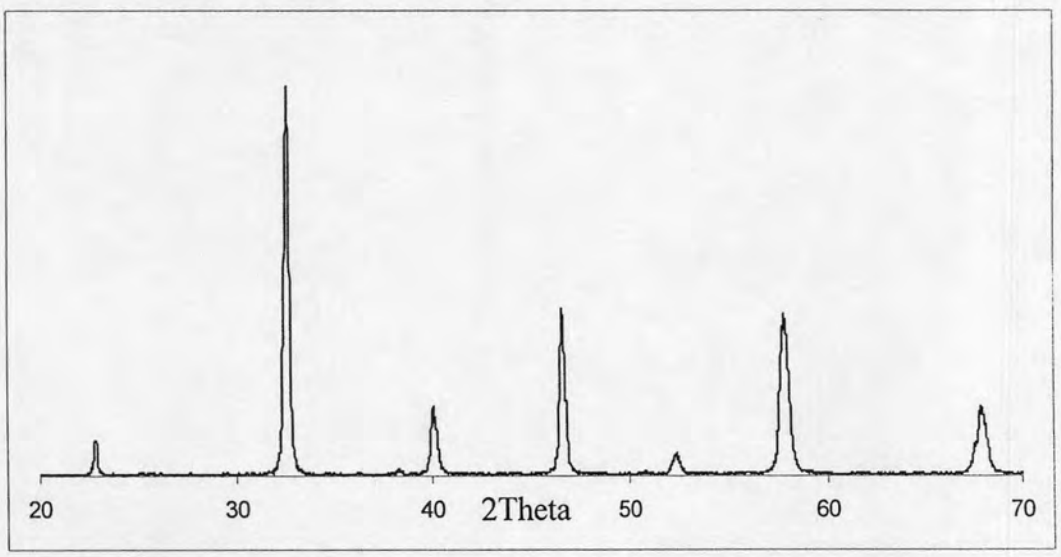

Figure 3.1 XRD pattern of $La_{0.7}Sr_{0.3}FeO_3$ powder after calcined at 1000°C for 6 hours.

The XRD pattern of LSF showed the single phase of ABO_3 perovskite oxide and a cubic structure with a space group P432 (Figure 3.1). From this Figure, the miller indexes were 100, 110, 111, 200, 210, 211 and 220 at 2θ = 22.8°, 32.4°, 40.0°, 46.5°, 52.4°, 57.9° and 67.9°, respectively. In addition, the lattice parameter calculated by Jade software is 3.900 A° and crystallite size is 32 nm from XRD line-broadening measurement from the Scherrer equation.

In this study, the effects of the dopants (Cu, Ni, Al and Mn) at Fe–site of $La_{0.7}Sr_{0.3}FeO_3$ on the structures were investigated.

3.2.1.2 Phase formation of $La_{0.7}Sr_{0.3}Fe_{1-x}Cu_xO_3$ (x=0.1 and 0.2)

XRD patterns of $La_{0.7}Sr_{0.3}Fe_{1-x}Cu_xO_3$ (x= 0, 0.1 and 0.2) powders were presented in Figure 3.2.

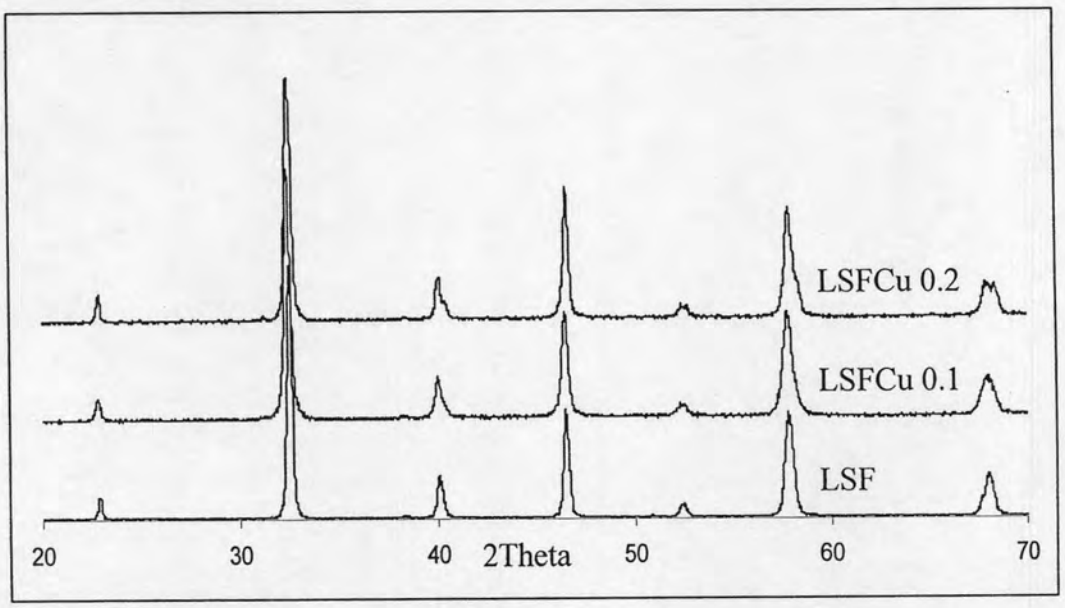

Figure 3.2 XRD patterns of $La_{0.7}Sr_{0.3}Fe_{1-x}Cu_xO_3$ (x = 0, 0.1 and 0.2) powders after calcined at 900-1000°C for 6 hours.

The XRD results indicated that Fe replaced by Cu 0.1 and 0.2 mol showed single phase and a cubic structure. XRD peaks of doped oxides shifted very slightly when compared with $La_{0.7}Sr_{0.3}FeO_3$, which ionic radius of Cu^{2+} (0.72 A°) is larger than Fe^{3+} (0.64 A°) but the lattice parameters of Cu–doped $La_{0.7}Sr_{0.3}FeO_3$ do not change significantly. The crystallite size of $La_{0.7}Sr_{0.3}Fe_{1-x}Cu_xO_3$ decreased by the substitution Cu for Fe as compared to that of undoped $La_{0.7}Sr_{0.3}FeO_3$.

Table 3.1 The lattice parameters and crystallite size of $La_{0.7}Sr_{0.3}Fe_{1-x}Cu_xO_3$ (x=0, 0.1 and 0.2) after calcined at 900–1000°C for 6 hours.

Sample	Lattice parameter (A°)	Crystallite size (nm)
$La_{0.7}Sr_{0.3}FeO_3$	3.900	32
$La_{0.7}Sr_{0.3}Fe_{0.9}Cu_{0.1}O_3$	3.902	25
$La_{0.7}Sr_{0.3}Fe_{0.8}Cu_{0.2}O_3$	3.896	24

3.2.1.3 Phase formation of $La_{0.7}Sr_{0.3}Fe_{1-x}Ni_xO_3$ (x=0.1, 0.2 and 0.3)

XRD patterns of $La_{0.7}Sr_{0.3}Fe_{1-x}Ni_xO_3$ (x= 0, 0.1, 0.2 and 0.3) powders were presented in Figure 3.3.

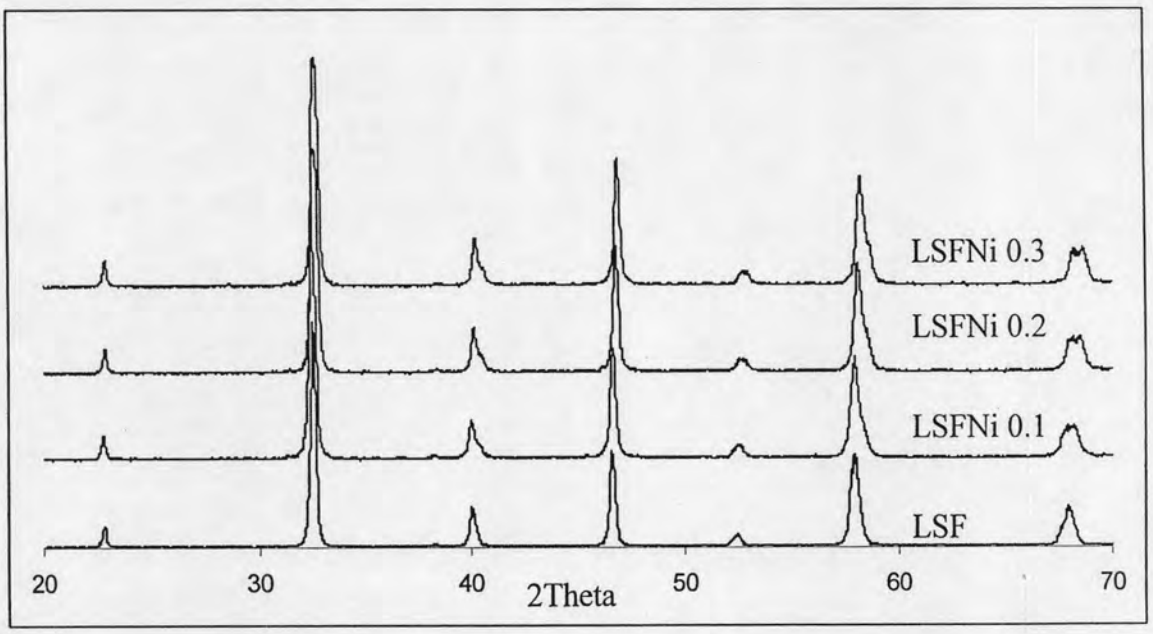

Figure 3.3 XRD pattern of $La_{0.7}Sr_{0.3}Fe_{1-x}Ni_xO_3$ (x= 0, 0.1, 0.2 and 0.3) powders after calcined at 1000°C for 6 hours.

As compared to $La_{0.7}Sr_{0.3}FeO_3$ sample, the diffraction peaks of Ni–substitution powder exhibited the tetragonal ABO_3 symmetry. It is shown that La^{3+} is substituted by Sr^{2+}, leads to the change of oxidation numbers at B site from Fe^{3+} to Fe^{4+}. When Fe site is partially substituted by Ni ions, it is considered that Ni^{2+}

changed to Ni^{3+}. Therefore, the distortion cubic structure of $La_{0.7}Sr_{0.3}FeO_3$ to tetragonal was observed and the cell volume of Ni–doped $La_{0.7}Sr_{0.3}FeO_3$ was smaller. Upon increase of doping amount of Ni the lattice parameters as well as the crystallite size (less than $La_{0.7}Sr_{0.3}FeO_3$) decreased as compared with those of $La_{0.7}Sr_{0.3}FeO_3$.

Table 3.2 The Lattice parameter and crystallite size of $La_{0.7}Sr_{0.3}Fe_{1-x}Ni_xO_3$ (x=0, 0.1, 0.2 and 0.3) after calcined at 1000°C for 6 hours.

Sample	Lattice parameter (A°)			Crystallite size (nm)
	a	b	c	
$La_{0.7}Sr_{0.3}FeO_3$	3.900	3.900	3.900	32
$La_{0.7}Sr_{0.3}Fe_{0.9}Ni_{0.1}O_3$	3.873	3.873	3.893	25
$La_{0.7}Sr_{0.3}Fe_{0.8}Ni_{0.2}O_3$	3.882	3.882	3.856	26
$La_{0.7}Sr_{0.3}Fe_{0.7}Ni_{0.3}O_3$	3.882	3.882	3.854	27

3.2.1.4 Phase formation of $La_{0.7}Sr_{0.3}Fe_{1-x}Al_xO_3$ (x=0.1, 0.2, 0.3 and 0.4)

XRD patterns of $La_{0.7}Sr_{0.3}Fe_{1-x}Al_xO_3$ (x=0, 0.1, 0.2, 0.3 and 0.4) powders were presented in Figure 3.4.

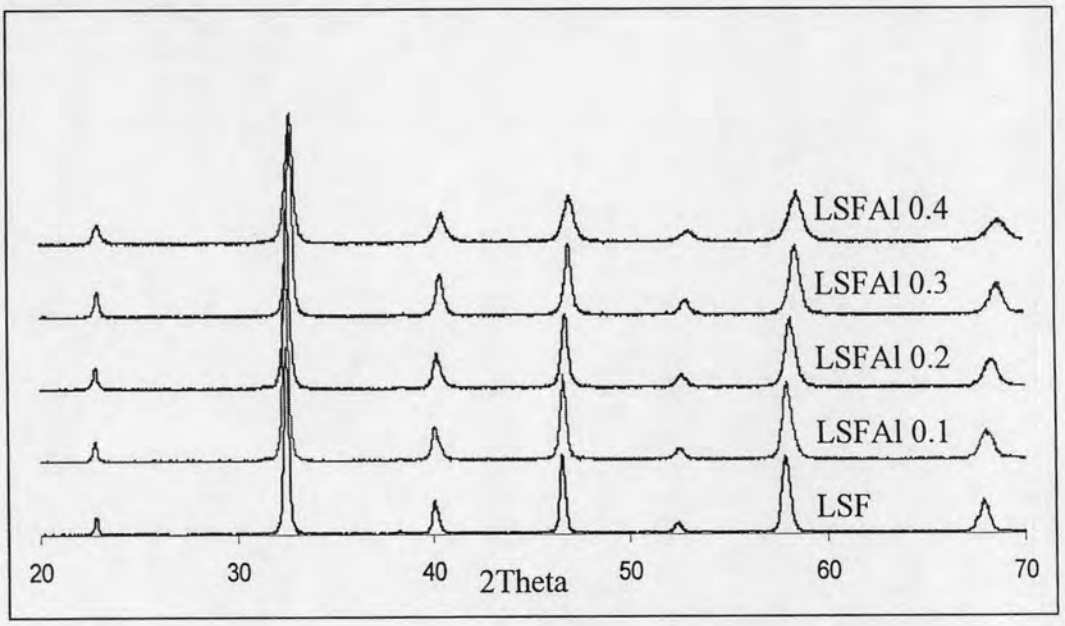

Figure 3.4 XRD pattern of $La_{0.7}Sr_{0.3}Fe_{1-x}Al_xO_3$ (x=0, 0.1, 0.2, 0.3 and 0.4) powders after calcined at 1000°C for 6 hours.

In Figure 3.4, the structures of perovskite doped by Al at B sites of $La_{0.7}Sr_{0.3}FeO_3$ are single phase with cubic perovskite structure. In addition, the XRD peaks slightly shifted to the higher angle compared with $La_{0.7}Sr_{0.3}FeO_3$. Table 3.3 showed that the lattice parameters of $La_{0.7}Sr_{0.3}FeO_3$ doping with Al at B site were less than that of $La_{0.7}Sr_{0.3}FeO_3$ because of smaller ionic radius of Al^{3+} (0.57 A°) partially replaced Fe^{3+} (0.64 A°). With increasing of Al, the pattern peaks shifted gradually to the high angle corresponding to the lattice shrinkage. The lattice parameters decreased with the increase amount of Al^{3+}. The crystallite size of Al–doped oxides were smaller than that of undoped material. It is shown that the increase of charge/size ratio of Al cause the cell volume to decrease.

Table 3.3 The lattice parameters and crystallite size of $La_{0.7}Sr_{0.3}Fe_{1-x}Al_xO_3$ (x=0, 0.1, 0.2, 0.3 and 0.4) after calcined at 1000°C for 6 hours.

Sample	Lattice parameter (A°)	Crystallite size (nm)
$La_{0.7}Sr_{0.3}FeO_3$	3.900	32
$La_{0.7}Sr_{0.3}Fe_{0.9}Al_{0.1}O_3$	3.886	27
$La_{0.7}Sr_{0.3}Fe_{0.8}Al_{0.2}O_3$	3.875	26
$La_{0.7}Sr_{0.3}Fe_{0.7}Al_{0.3}O_3$	3.864	26
$La_{0.7}Sr_{0.3}Fe_{0.6}Al_{0.4}O_3$	3.850	25

3.2.1.5 Phase formation of $La_{0.7}Sr_{0.3}Fe_{1-x}Mn_xO_3$ (x=0.1 and 0.2)

XRD patterns of $La_{0.7}Sr_{0.3}Fe_{1-x}Mn_xO_3$ (x=0, 0.1 and 0.2) oxides were presented in Figure 3.5.

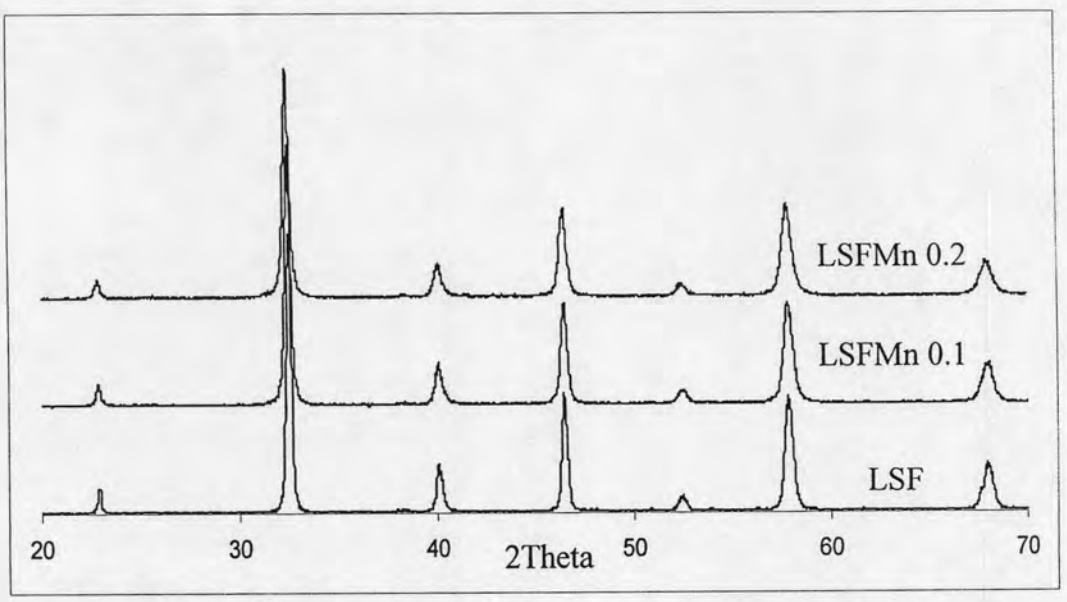

Figure 3.5 XRD pattern of $La_{0.7}Sr_{0.3}Fe_{1-x}Mn_xO_3$ (x = 0, 0.1 and 0.2) powders after calcined at 1000°C for 6 hours.

Figure 3.5 shows the XRD patterns of $La_{0.7}Sr_{0.3}Fe_{0.9}Mn_{0.1}O_3$ and $La_{0.7}Sr_{0.3}Fe_{0.8}Mn_{0.2}O_3$. It demonstrated that all samples doping with Mn^{2+} in the B sites of $La_{0.7}Sr_{0.3}FeO_3$ have no any impurity phase and the structures are cubic. The XRD patterns of Mn–doped oxides shifted slightly to the lower angle as compared with $La_{0.7}Sr_{0.3}FeO_3$. Theoretically, when the larger ions of Mn^{3+} (0.66 A°) is partially

replaced into Fe^{3+} and Fe^{4+} site the lattice volume should expand. But the lattice parameters of Mn-doped $La_{0.7}Sr_{0.3}FeO_3$ does not change significantly as compared to $La_{0.7}Sr_{0.3}FeO_3$. However, only 20% of Mn ion can be doped into Fe site without distortion of the ABO_3 structure.

Table 3.4 The lattice parameters crystallite size of $La_{0.7}Sr_{0.3}Fe_{1-x}Mn_xO_3$ (x=0.1 and 0.2) after calcined at 1000°C for 6 hours.

Sample	Lattice parameter (A°)	Crystallite size (nm)
$La_{0.7}Sr_{0.3}FeO_3$	3.900	32
$La_{0.7}Sr_{0.3}Fe_{0.9}Mn_{0.1}O_3$	3.898	27
$La_{0.7}Sr_{0.3}Fe_{0.8}Mn_{0.2}O_3$	3.900	25

3.3.2 Scanning electron microscope (SEM) and density

The morphologies of perovskite disc were examined by SEM technique. The grain sizes of metals-doped $La_{0.7}Sr_{0.3}FeO_3$ were compared with an undoped oxide. Densities of samples were determined by the Archimedes immersion method using water as a medium.

3.3.2.1 The morphology of $La_{0.7}Sr_{0.3}FeO_3$

The surface morphology of $La_{0.7}Sr_{0.3}FeO_3$ disc after sintered at 1300°C for 10 hours was shown in Figure 3.6.

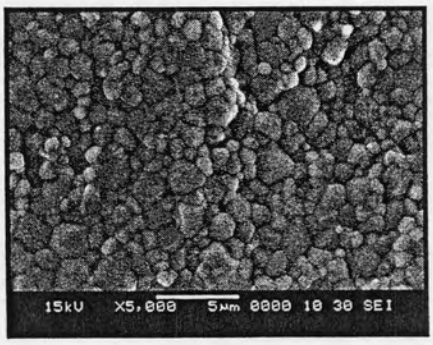

Figure 3.6 Surface morphology of $La_{0.7}Sr_{0.3}FeO_3$ disc.

SEM micrograph of $La_{0.7}Sr_{0.3}FeO_3$ disc exhibited high density (5.8993 $g.cm^3$ and relative density is 92.6 %) and homogenous phase. The rough grain sizes of perovskite disc are in the range of 1–3 μm. This grain size data was directly estimated from SEM micrograph.

3.3.2.2 The morphology of $La_{0.7}Sr_{0.3}Fe_{1-x}Cu_xO_3$ (x=0.1 and 0.2)

The surface morphology of $La_{0.7}Sr_{0.3}Fe_{1-x}Cu_xO_3$ disc after sintered at 1,100°C for 10 hours were shown in Figure 3.7.

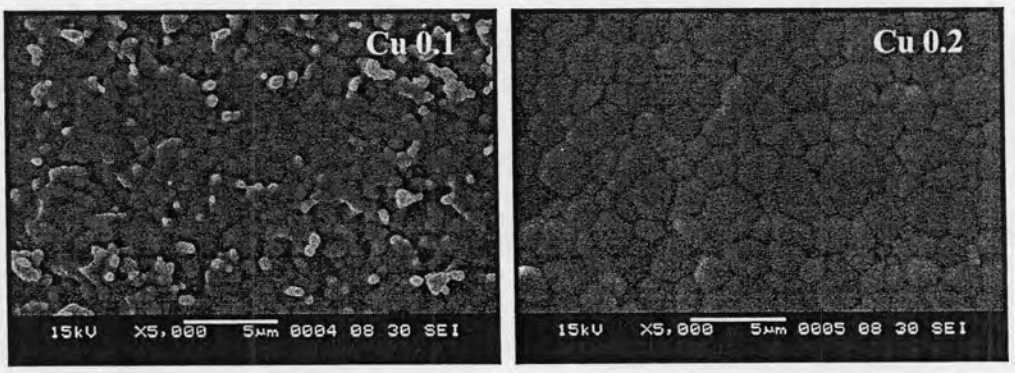

Figure 3.7 Surface morphology of $La_{0.7}Sr_{0.3}Fe_{1-x}Cu_xO_3$ (x=0.1, 0.2) disc.

The grain size slightly increased with the increasing content of Cu. The average grain size for the $La_{0.7}Sr_{0.3}Fe_{0.9}Cu_{0.1}O_3$ and $La_{0.7}Sr_{0.3}Fe_{0.8}Cu_{0.2}O_3$ discs are about 1μm and 3–5 μm, respectively. As observed previously [26-27] the increase in particle size with the doping level is a result of a change in the melting point of the samples. Doping with copper decreases melting points of the materials, this effect results in an enhanced grain growth.

The densities of $La_{0.7}Sr_{0.3}Fe_{1-x}Cu_xO_3$ with various amounts of Cu were listed in Table 3.5. $La_{0.7}Sr_{0.3}Fe_{0.9}Cu_{0.2}O_3$ has the highest density.

Table 3.5 Density of $La_{0.7}Sr_{0.3}Fe_{1-x}Cu_xO_3$ discs when x = 0.1 and 0.2.

$La_{0.7}Sr_{0.3}Fe_{1-x}Cu_xO_3$ disc	Density/g.cm^3	Relative density (%)
$La_{0.7}Sr_{0.3}Fe_{0.9}Cu_{0.1}O_3$	5.8101	91.1
$La_{0.7}Sr_{0.3}Fe_{0.8}Cu_{0.2}O_3$	5.9833	93.0

3.3.2.3 The morphology of $La_{0.7}Sr_{0.3}Fe_{1-x}Ni_xO_3$ (x=0.1, 0.2 and 0.3)

The surface of $La_{0.7}Sr_{0.3}Fe_{1-x}Ni_xO_3$ discs were investigated by SEM technique shown in Figure 3.8.

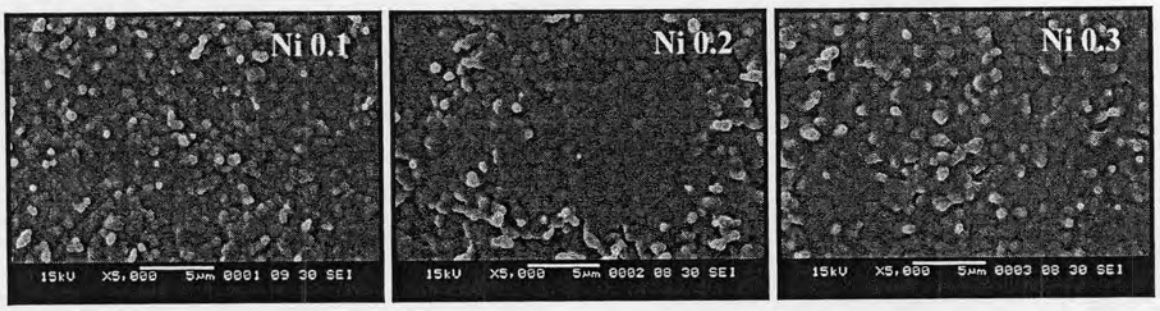

Figure 3.8 Surface morphology of $La_{0.7}Sr_{0.3}Fe_{1-x}Ni_xO_3$ (x=0.1, 0.2 and 0.3) disc.

It is observed that the grain size of Ni-doped $La_{0.7}Sr_{0.3}FeO_3$ is smaller than that of $La_{0.7}Sr_{0.3}FeO_3$. The increase amount of Ni substituted at Fe site has no effect on the grain size. The average grain size of $La_{0.7}Sr_{0.3}Fe_{1-x}Ni_xO_3$ (x=0.1, 0.2 and 0.3) are about 0.8-1 μm for each content of Ni.

The densities of $La_{0.7}Sr_{0.3}Fe_{1-x}Ni_xO_3$ discs increase with the increase of Ni which was listed in Table 3.6.

Table 3.6 Density of $La_{0.7}Sr_{0.3}Fe_{1-x}Ni_xO_3$ discs when x = 0.1, 0.2 and 0.3.

$La_{0.7}Sr_{0.3}Fe_{1-x}Ni_xO_3$ disc	Density/g.cm^3	Relative density (%)
$La_{0.7}Sr_{0.3}Fe_{0.9}Ni_{0.1}O_3$	5.6592	87.4
$La_{0.7}Sr_{0.3}Fe_{0.8}Ni_{0.2}O_3$	5.8361	89.6
$La_{0.7}Sr_{0.3}Fe_{0.7}Ni_{0.3}O_3$	5.9405	91.0

3.3.2.4 The morphology of $La_{0.7}Sr_{0.3}Fe_{1-x}Al_xO_3$ (x=0.1, 0.2, 0.3 and 0.4)

Fig. 3.9 shows the SEM micrographs of $La_{0.7}Sr_{0.3}Fe_{1-x}Al_xO_3$ (x = 0.1, 0.2, 0.3 and 0.4) disc sintered at 1300°C for 10 h.

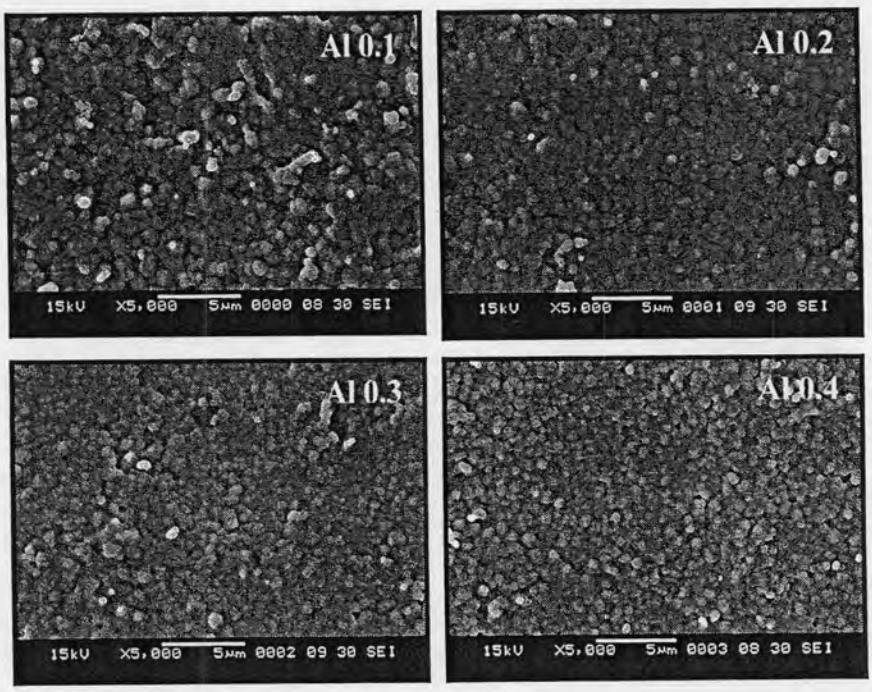

Figure 3.9 Surface morphology of $La_{0.7}Sr_{0.3}Fe_{1-x}Al_xO_3$ (x = 0.1, 0.2, 0.3 and 0.4) disc.

The observed morphology reveals uniform surface of these materials. The grain sizes of Al–doped $La_{0.7}Sr_{0.3}FeO_3$ are smaller than that of undoped $La_{0.7}Sr_{0.3}FeO_3$ and pore sizes increased with an increasing content of Al. The average grain size for the $La_{0.7}Sr_{0.3}Fe_{0.9}Al_{0.1}O_3$, $La_{0.7}Sr_{0.3}Fe_{0.8}Al_{0.2}O_3$, $La_{0.7}Sr_{0.3}Fe_{0.7}Al_{0.3}O_3$ and $La_{0.7}Sr_{0.3}Fe_{0.6}Al_{0.4}O_3$ disc are about 1 μm, 0.8 μm, 0.6 μm and 0.5 μm, respectively.

In addition, the large closed pores caused the decrease of the disc density. Therefore, the density of $La_{0.7}Sr_{0.3}Fe_{1-x}Al_xO_3$ gradually decreased with Al contents, were listed in Table 3.7.

Table 3.7 Density of $La_{0.7}Sr_{0.3}Fe_{1-x}Al_xO_3$ discs when x = 0.1, 0.2, 0.3 and 0.4.

$La_{0.7}Sr_{0.3}Fe_{1-x}Al_xO_3$ disc	Density/g.cm^3	Relative density (%)
$La_{0.7}Sr_{0.3}Fe_{0.9}Al_{0.1}O_3$	5.9895	94.2
$La_{0.7}Sr_{0.3}Fe_{0.8}Al_{0.2}O_3$	5.8447	92.4
$La_{0.7}Sr_{0.3}Fe_{0.7}Al_{0.3}O_3$	5.1575	81.9
$La_{0.7}Sr_{0.3}Fe_{0.6}Al_{0.4}O_3$	4.7718	76.0

3.3.2.5 The morphology of $La_{0.7}Sr_{0.3}Fe_{1-x}Mn_xO_3$ (x=0.1, 0.2)

Fig. 3.10 shows the SEM micrographs of $La_{0.7}Sr_{0.3}Fe_{1-x}Mn_xO_3$ (x = 0.1 and 0.2) disc sintered at 1300°C for 10 h.

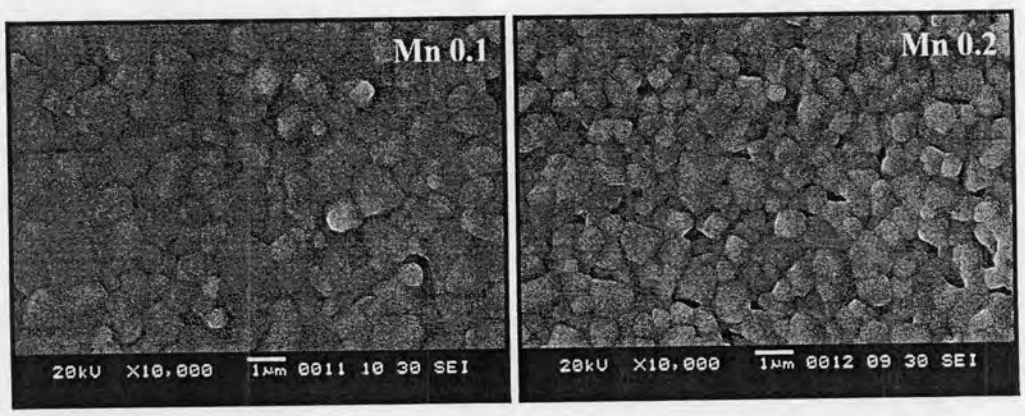

Figure 3.10 Surface morphology of $La_{0.7}Sr_{0.3}Fe_{1-x}Mn_xO_3$ (x=0.1, 0.2) disc.

The grain sizes of Mn–doped $La_{0.7}Sr_{0.3}FeO_3$ (1 μm) are about the same as that of $La_{0.7}Sr_{0.3}FeO_3$. It is suggested that doping Mn ion at Fe site does not affect the grain size.

The densities of $La_{0.7}Sr_{0.3}Fe_{1-x}Mn_xO_3$ decrease with the increase amounts of Mn. (see Table 3.8)

Table 3.8 Density of $La_{0.7}Sr_{0.3}Fe_{1-x}Mn_xO_3$ discs when x = 0.1, and 0.2.

$La_{0.7}Sr_{0.3}Fe_{1-x}Mn_xO_3$ disc	Density/g.cm^3	Relative density (%)
$La_{0.7}Sr_{0.3}Fe_{0.9}Mn_{0.1}O_3$	5.8914	92.4
$La_{0.7}Sr_{0.3}Fe_{0.8}Mn_{0.2}O_3$	5.1311	80.6

3.3.3 Temperature–Programmed reduction (TPR)

Temperature-programmed reduction (TPR) is a technique for the characterization of solid materials and is often used in the field of heterogeneous catalysis to find the most efficient reduction conditions. TPR experiments were measured using H_2/Ar temperature–programmed reduction. The sintered perovskite powder was first pretreated in O_2 atmosphere (30 ml/min) at 500°C for 1 hours, then cooling in flowing O_2 down to 100°C, and thereafter reduced with 5% H_2/Ar mixture heating 10°C/min up to 900°C gas mixture was employed for recording of the reduction profiles. Water produced by the sample reduction was condensed in a cold trap before reaching the detectors. Only H_2 was detected in the outlet gas confirming the effectiveness of the cold trap.

The reduction profiles (TPR) of metals-doped $La_{0.7}Sr_{0.3}FeO_3$ were preformed in this work except $La_{0.7}Sr_{0.3}FeO_3$.

3.3.3.1 Reducibility of $La_{0.7}Sr_{0.3}FeO_3$ compound

The structure of $La_{0.8}Sr_{0.2}FeO_3$ which is similar to $La_{0.7}Sr_{0.3}FeO_3$ was used as reference material for TPR consideration.

N.M Gupta *et al.* [28] reported the reducibility of $La_{0.8}Sr_{0.2}FeO_3$ investigated by H_2–TPR experiments, as illustrated in Figure 3.11.

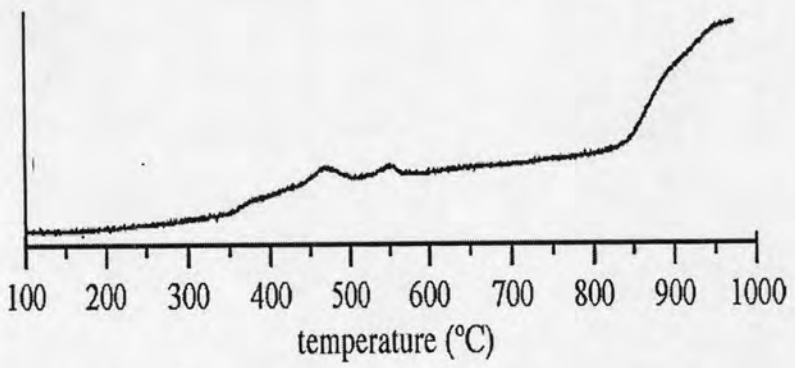

Figure 3.11 H_2–TPR profiles of $La_{0.8}Sr_{0.2}FeO_3$ compound.

Because La^{3+} and Sr^{2+} is nonreducible under the conditions of H_2-TPR, the observed H_2 consumption should be ascribed to the reduction of Fe^{n+} ions in the case of $La_{0.8}Sr_{0.2}FeO_3$ and when La^{3+} is substituted by Sr^{2+}, leads to the change of

oxidation numbers at B site from Fe^{3+} to Fe^{4+}. A small amount of highly reducible Fe^{4+} has been reported in $LaFeO_3$ [29–31], and its reduction to Fe^{3+} occurred at T <300°C during H_2–TPR experiments [30]. The small amount of H_2 consumed at 370°C in the H_2–TPR profile of $La_{0.8}Sr_{0.2}FeO_3$ can be attributed to the reduction of Fe^{4+} to Fe^{3+}, followed by a successive reduction of Fe^{3+} centered at 460 and 550°C, respectively. The quantitative analysis of these two peaks correlated well with the H_2 consumption in the reduction of Fe^{3+} to Fe^{2+}. They were therefore ascribed to $Fe^{3+}\rightarrow Fe^{2+}$ reduction occurring over the surface and in the bulk of $La_{0.8}Sr_{0.2}FeO_3$, respectively. Subsequently, the minor reduction peak above 800°C was assigned to the partial reduction of Fe^{2+} to metallic iron [32].

3.3.3.2 Reducibility of $La_{0.7}Sr_{0.3}Fe_{1-x}Cu_xO_3$ (x=0.1 and 0.2)

The reduction profiles (TPR) of $La_{0.7}Sr_{0.3}FeO_3$ along with its coppers substituted homologues are presented in Figure 3.12

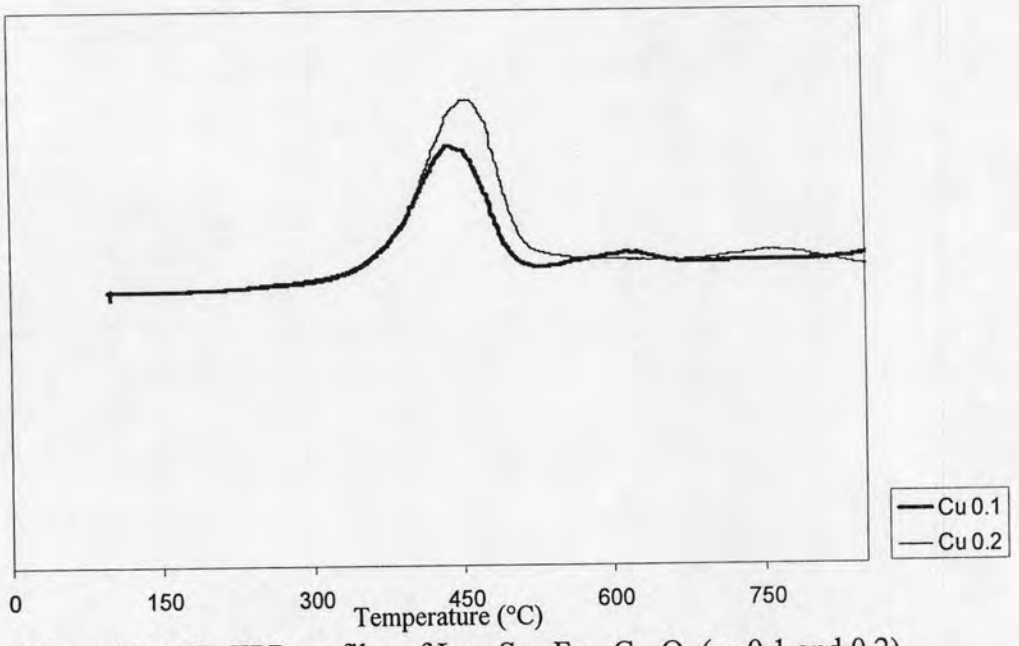

Figure 3.12 H_2-TPR profiles of $La_{0.7}Sr_{0.3}Fe_{1-x}Cu_xO_3$ (x=0.1 and 0.2)

The reduction profile of $La_{0.7}Sr_{0.3}Fe_{0.9}Cu_{0.1}O_3$ and $La_{0.7}Sr_{0.3}Fe_{0.8}Cu_{0.2}O_3$ exhibits two broad signals at 450 and 460°C, respectively. These TPR profiles might be due to the overlapping band of reduction of Fe^{4+} to Fe^{3+}, Fe^{3+} to Fe^{2+} (over the surface) and Cu^{2+} to Cu^{+}. The additional peak at 550-670°C for $La_{0.7}Sr_{0.3}Fe_{0.9}Cu_{0.1}O_3$

is reduction occurring in the bulk of Fe^{3+} to Fe^{2+}. The low intensity at high temperatures (> 800°C) indicates the reduction of Cu^{+} to Cu^{0} and Fe^{2+} to metallic iron. In case of $La_{0.7}Sr_{0.3}Fe_{0.8}Cu_{0.2}O_3$, the reduction of Cu^{+} to Cu^{0} and Fe^{2+} to metallic iron occurs at 710–830°C. When the composition of Cu changed from 10% to 20%, the reduction peaks shifted gradually to lower temperatures. It is evident that doping Cu at Fe site causes the perovskite oxide to be more easily reducible [45].

3.3.3.3 Reducibility of $La_{0.7}Sr_{0.3}Fe_{1-x}Ni_xO_3$ (x=0.1, 0.2 and 0.3)

The reduction profiles (TPR) of $La_{0.7}Sr_{0.3}FeO_3$ along with its nickels substituted homologues are presented in Figure 3.13

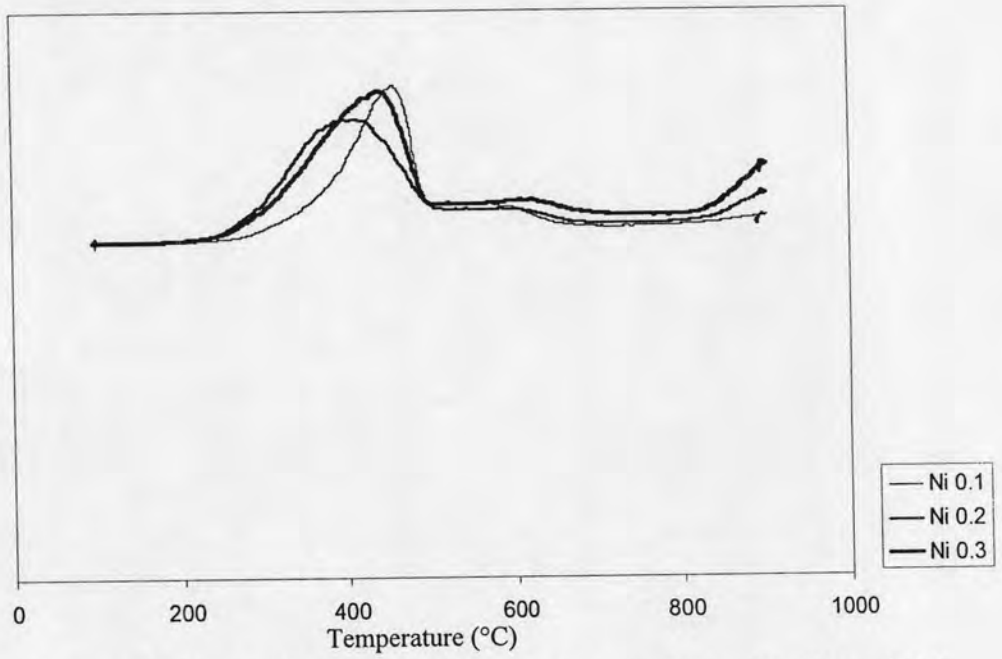

Figure 3.13 H_2–TPR profiles of $La_{0.7}Sr_{0.3}Fe_{1-x}Ni_xO_3$ (x=0.1, 0.2 and 0.3)

For the $La_{0.7}Sr_{0.3}Fe_{1-x}Ni_xO_3$ perovskite type series, the TPR profiles are displayed in Figure 3.13. It is observed that the first reduction event takes place at low temperatures between 200–460°C which is due to the reduction of Fe^{4+} to Fe^{3+}, Fe^{3+} to Fe^{2+} (over the surface), Ni^{4+} to Ni^{3+} and Ni^{3+} to Ni^{2+}. The shoulders appeared around 500–700°C are ascribed to the reduction of Ni^{2+} to Ni^{0} and Fe^{3+} to Fe^{2+} reduction in the bulk (second step). It is apparent that the TPR peaks of Ni–doped oxide shifted to lower temperature (200°C) as compare to that of undoped material, suggesting that the Ni–substitution at Fe site might facilitate the reduction. Additionally,

the minor reduction peak above 800°C was assigned to the partial reduction of Fe^{2+} to metallic iron. The non–stoichiometric Ni–based perovskite–like oxides are able to stabilize Ni^{2+} and Ni^{+} particles, accounting for incomplete reduction and some difficulty in accurately determining hydrogen consumption [33].

3.3.3.4 Reducibility of $La_{0.7}Sr_{0.3}Fe_{1-x}Al_xO_3$ (x=0.1, 0.2, 0.3 and 0.4)

The reduction profiles (TPR) of $La_{0.7}Sr_{0.3}FeO_3$ along with its aluminums substituted homologues are presented in Figure 3.14

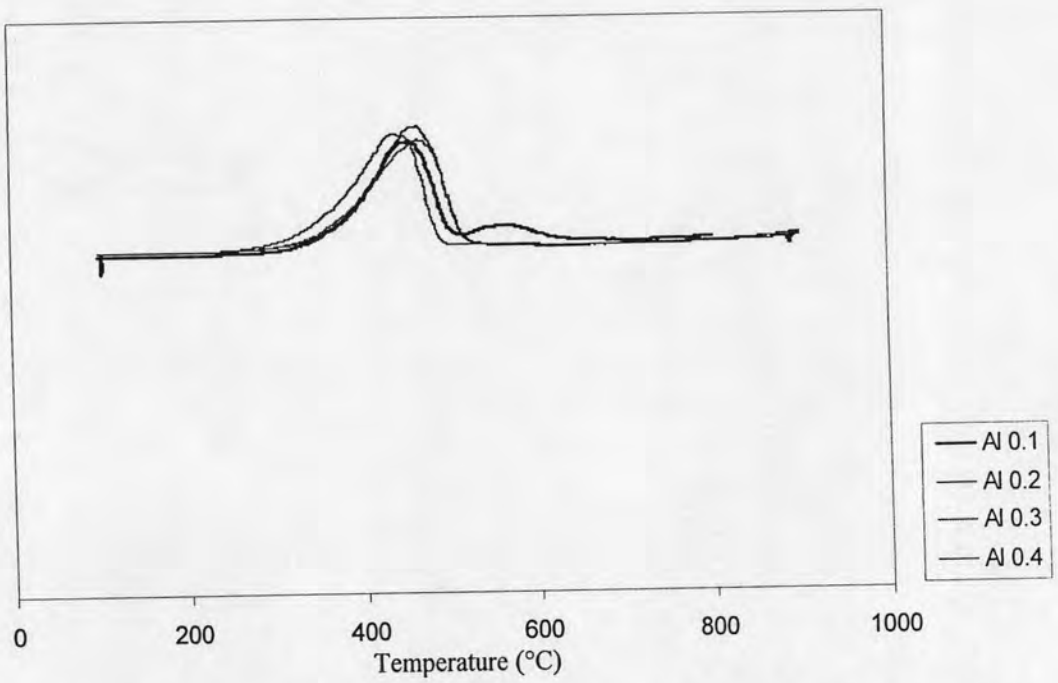

Figure 3.14 H_2–TPR profiles of $La_{0.7}Sr_{0.3}Fe_{1-x}Al_xO_3$ (x=0.1, 0.2, 0.3 and 0.4)

Because Al^{3+} is nonreducible under the conditions of H_2-TPR, the observed H_2 consumption should be ascribed to the reduction of Fe^{n+} ions in the case of $La_{0.7}Sr_{0.3}Fe_{1-x}Al_xO_3$. The reduction profile of $La_{0.7}Sr_{0.3}Fe_{0.9}Al_{0.1}O_3$ centered at 457°C corresponding to the overlapping of reduction peaks of Fe^{4+} to Fe^{3+} and Fe^{3+} to Fe^{2+} (over the surface) and showed a small peak in the temperature interval of 520–640°C might be ascribed to the reduction of Fe^{3+} to Fe^{2+} in the bulk of $La_{0.7}Sr_{0.3}Fe_{0.9}Al_{0.1}O_3$. The low intensity of TPR bands at above 850°C indicated the reduction of Fe^{2+} to metallic iron. When of Al is more than 10%, the maximum temperature for reduction changed somewhat which cannot be concluded.

3.3.3.5 Reducibility of $La_{0.7}Sr_{0.3}Fe_{1-x}Mn_xO_3$ (x=0.1 and 0.2)

The reduction profiles (TPR) of $La_{0.7}Sr_{0.3}FeO_3$ along with its manganese substituted homologues are presented in Figure 3.15

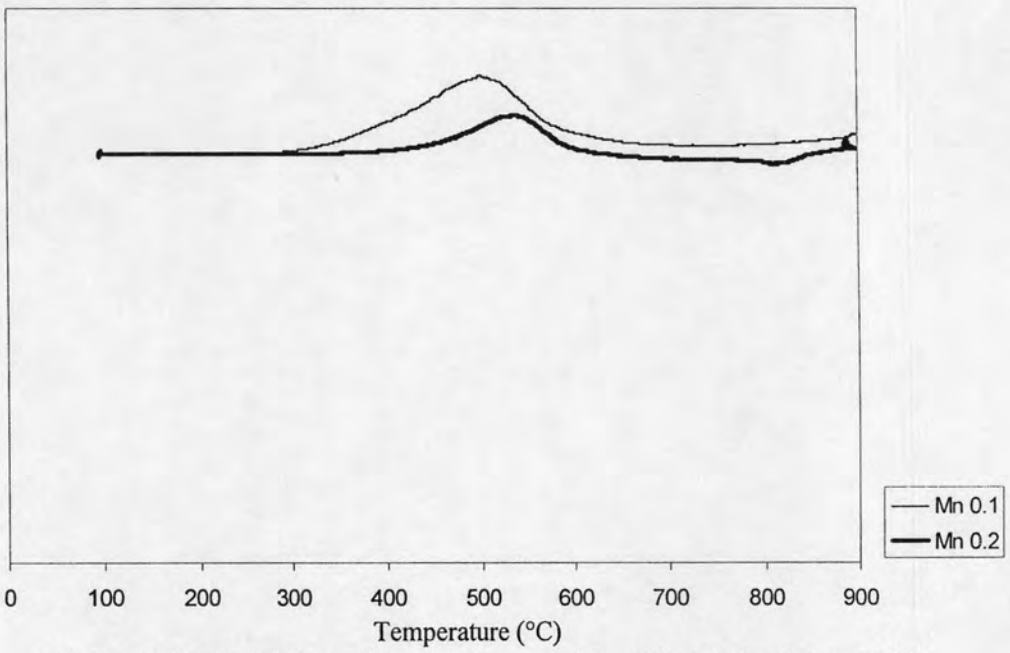

Figure 3.15 H_2–TPR profiles of $La_{0.7}Sr_{0.3}Fe_{1-x}Mn_xO_3$ (x=0.1 and 0.2)

The reduction profile of $La_{0.7}Sr_{0.3}Fe_{0.9}Mn_{0.1}O_3$ and $La_{0.7}Sr_{0.3}Fe_{0.8}Mn_{0.2}O_3$ showed the center at 510 and 545°C, respectively, due to the reduction of Mn^{3+} to Mn^{2+}, Fe^{4+} to Fe^{3+} and Fe^{3+} to Fe^{2+} ions. It has been demonstrated by Gupta *et al.* that Mn is present in +4 as well as in +3 states and Mn^{4+} ion reduces at a lower temperature (<500°C) than Mn^{3+} ion[28]. With increasing of Mn, the reduction peaks shifted to higher temperatures indicating an increase of Mn^{3+}. The low intensity of TPR bands at high temperatures revealed that the reduction of Fe^{2+} to metallic iron might occur only at temperatures above 800°C.

3.3.4 Electrical Conductivity Measurement

The total electrical conductivities of the obtained oxides as a function of temperature were measured by the DC 4–probes method. The measured value of total conductivity includes electronic and ionic contributions due to the presence of charge carriers and oxygen vacancies, respectively. However, ionic conductivity in the type of perovskite oxides is known to be small in comparison with the overall conductivity [34]. Therefore, the experimental value of the electrical conductivity is assumed to be the electronic conductivity alone.

The electrical conductivity is strongly dependent on temperature. The electrical conductivity of metals decreases with increasing temperature whereas the electrical conductivity of semiconductors increases with increasing temperature.

Electrical conductivities of the $La_{0.7}Sr_{0.3}Fe_{1-x}M_xO_3$ (M= Cu, x= 0.1 and 0.2; M= Ni, x= 0.1, 0.2 and 0.3; M= Al, x= 0.1, 0.2, 0.3 and 0.4; M= Mn, x= 0.1 and 0.2) anodes were determined from room temperature to 800°C in air.

3.3.4.1 Electrical conductivity of $La_{0.7}Sr_{0.3}FeO_3$ compound

The electrical conducting property of $La_{0.7}Sr_{0.3}FeO_3$ was investigated as a function of temperature.

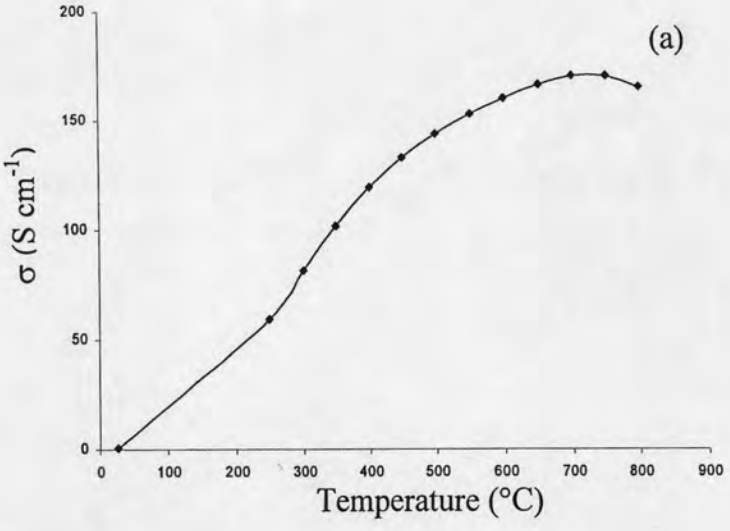

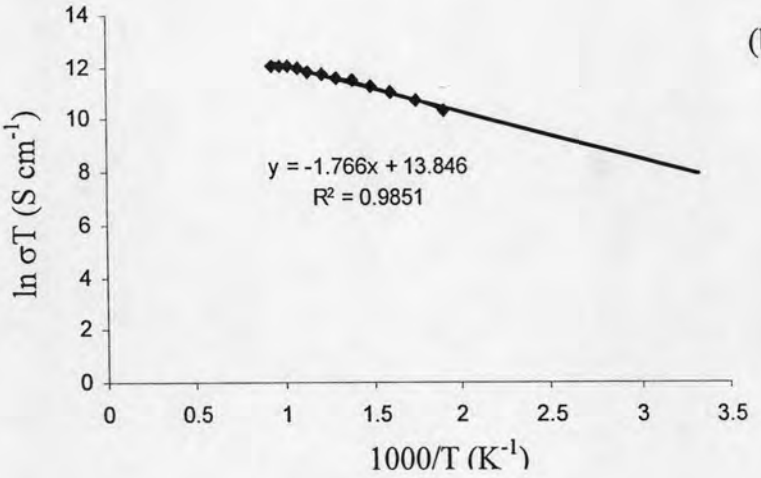

Figure 3.16 (a) Temperature dependence of the electrical conductivity (σ) for $La_{0.7}Sr_{0.3}FeO_3$.

(b) Arrhenius plot of the electrical conductivity of $La_{0.7}Sr_{0.3}FeO_3$.

Figure 3.16 (a) shows the temperature dependence of the electrical conductivity (σ) for $La_{0.7}Sr_{0.3}FeO_3$ ceramic. The electrical conductivity increases with temperature until reaching a maximum value of 170 S/cm at 750°C and then decreases. The Arrhenius plot of $La_{0.7}Sr_{0.3}FeO_3$ is given in Figure 3.16 (b). Its linear part can be described by the small polaron conduction mechanism, following the formula: $\sigma = (A/T) \exp(-E_a/kT)$, where A is material constant including the carrier concentration term, E_a is the activation energy, k is the Boltzmann's constant and T is the absolute temperature. The activation energy calculated from the linear part of Figure 3.16 (b) is 14.68 kJ/mol. The specimen displays an obvious transition in electrical conduction characteristic *p*–type semiconductor.

For Sr–doped lanthanum metal oxide ($La_{1-x}Sr_xMO_{3-\delta}$), when lanthanum lattice sites were occupied by strontium ions, negative effective charges (Sr'_{La}) were formed. These negative effective charges must be compensated by the formation of equivalent amount of positive effective charges, such as electron holes ($h^{\bullet}$) or oxygen vacancies ($V_o^{\bullet\bullet}$). The following defect reactions may be used to describe the addition of SrO and MO into the $LaMO_3$ lattice depending upon the defects generated from charge compensation:

$$\frac{1}{2}O_2 + 2SrO + 2MO \xrightarrow[LaMO_3]{} 2Sr'_{La} + 2M^x_M + 5O^x_O + V_O^{\bullet\bullet} \quad (1)$$

$$O_2 + 2SrO + 2MO \xrightarrow[LaMO_3]{} 2Sr'_{La} + 2M^x_M + 6O^x_O + 2h^{\bullet} \quad (2)$$

where Sr'_{La} represents the substitution of Sr for La cation sublattice and M^x_M indicates that the M ions is located at the M-cation sublattice [12]. This research work is aiming to enhance the electrical conductivities of the $La_{0.7}Sr_{0.3}FeO_3$ material by B site substitution (Cu, Ni, Al and Mn).

3.3.4.2 Electrical conductivity of $La_{0.7}Sr_{0.3}Fe_{1-x}Cu_xO_3$ (x=0.1 and 0.2)

The temperature dependence of the electrical conductivities of the $La_{0.7}Sr_{0.3}Fe_{1-x}Cu_xO_3$ (x=0.1 and 0.2) samples are shown in Figure 3.17 and Table 3.9.

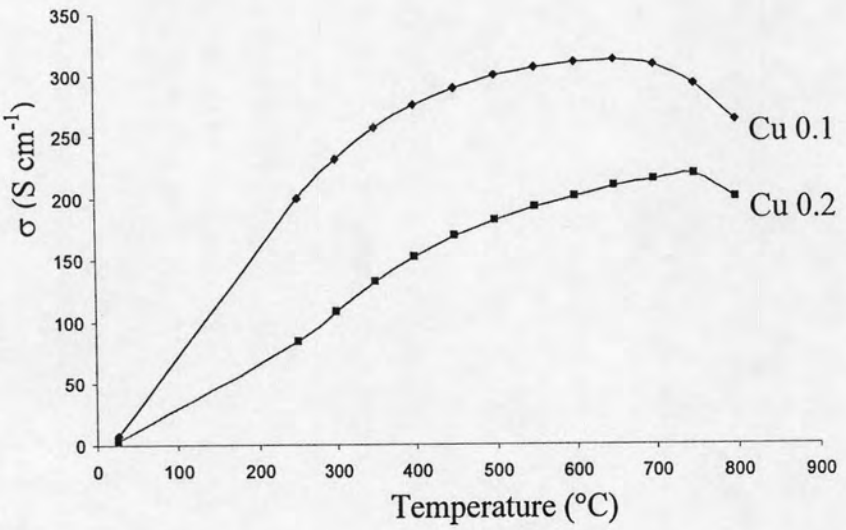

Figure 3.17 Temperature dependence of the electrical conductivity (σ) for $La_{0.7}Sr_{0.3}Fe_{1-x}Cu_xO_3$ (x=0.1 and 0.2)

Table 3.9 Specific conductivity of $La_{0.7}Sr_{0.3}Fe_{1-x}Cu_xO_3$ (x=0.1 and 0.2).

Sample	Specific conductivity, σ (S/cm)						
	300°C	400°C	500°C	600°C	700°C	800°C	σ_{max} (T,°C)
$La_{0.7}Sr_{0.3}Fe_{0.9}Cu_{0.1}O_3$	230.9	275.4	299.6	310.4	308.4	262.6	312.2 (650)
$La_{0.7}Sr_{0.3}Fe_{0.8}Cu_{0.2}O_3$	108.4	152.7	181.7	200.6	214.8	199.4	218.5 (750)

It is found that the conductivities of Cu–doped $La_{0.7}Sr_{0.3}FeO_3$ species increase with an increase of temperature (semi-conductivity) and the conductivity of $La_{0.7}Sr_{0.3}Fe_{0.9}Cu_{0.1}O_3$ reaches the maximum value of 312.2 S/cm at about 650°C and begins to decrease. As compared to that of undoped $La_{0.7}Sr_{0.3}FeO_3$, the conductivity of the sample significantly increased by the substitution of Cu for Fe. When the amount of Cu changes from 10% to 20%, the maximum conductivity exists at the higher temperature and the value becomes lower (218.5 S/cm). It can be interpreted in term of grain size. It is validated by the SEM micrograph that the grain size of 20% Cu–doped material is considerably larger than the former.

Shown in Table 3.10, the activation energies of Cu specimens are less than that of $La_{0.7}Sr_{0.3}FeO_3$ and tend to increase with the Cu amount.

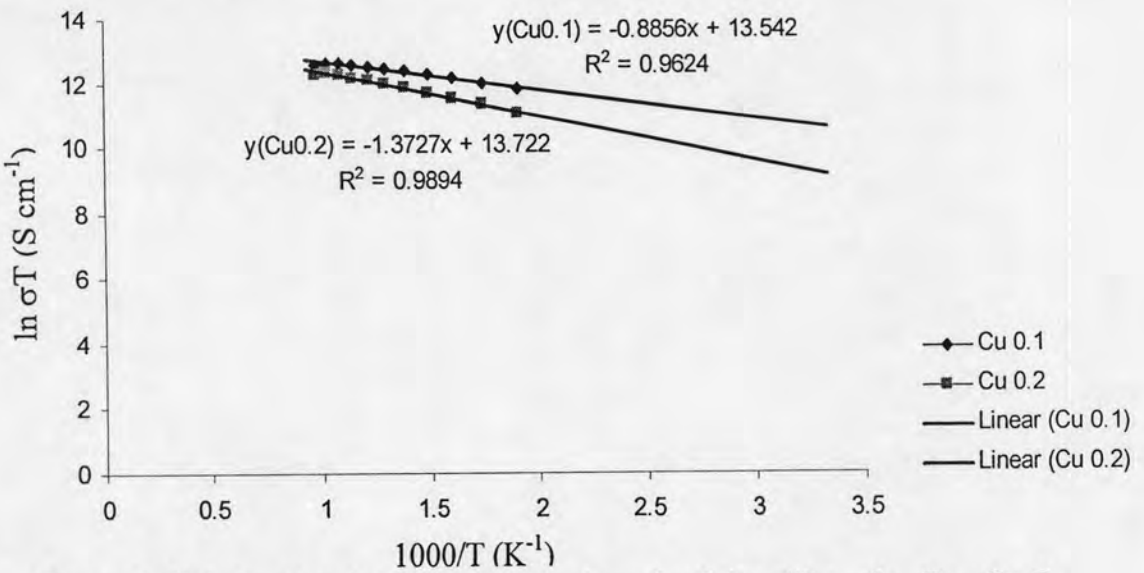

Figure 3.18 Arrhenius plot of the electrical conductivity of $La_{0.7}Sr_{0.3}Fe_{1-x}Cu_xO_3$ (x=0.1 and 0.2).

Table 3.10 Activation energy of $La_{0.7}Sr_{0.3}FeO_3$ and $La_{0.7}Sr_{0.3}Fe_{1-x}Cu_xO_3$ (x=0.1 and 0.2).

Sample	E_a (kJ/mol)
$La_{0.7}Sr_{0.3}FeO_3$	14.68
$La_{0.7}Sr_{0.3}Fe_{0.9}Cu_{0.1}O_3$	9.02
$La_{0.7}Sr_{0.3}Fe_{0.8}Cu_{0.2}O_3$	13.76

3.3.4.3 Electrical conductivity of $La_{0.7}Sr_{0.3}Fe_{1-x}Ni_xO_3$ (x=0.1, 0.2 and 0.3)

The temperature dependence of the electrical conductivitis of the $La_{0.7}Sr_{0.3}Fe_{1-x}Ni_xO_3$ (x=0.1, 0.2 and 0.3) samples are shown in Figure 3.19 and Table 3.11.

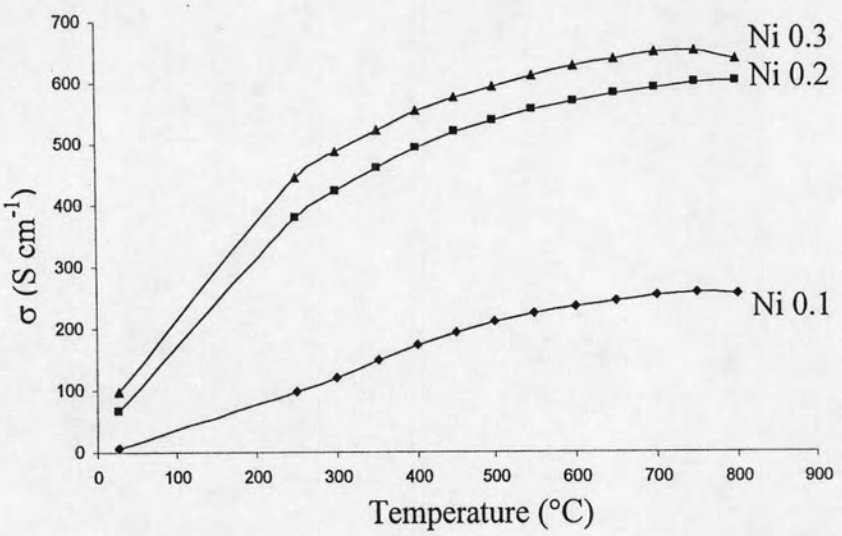

Figure 3.19 Temperature dependence of the electrical conductivity (σ) for $La_{0.7}Sr_{0.3}Fe_{1-x}Ni_xO_3$ (x=0.1, 0.2 and 0.3).

Table 3.11 Specific conductivity of $La_{0.7}Sr_{0.3}Fe_{1-x}Ni_xO_3$ (x=0.1, 0.2 and 0.3).

Sample	Specific conductivity, σ (S/cm)						
	300°C	400°C	500°C	600°C	700°C	800°C	σ_{max} (T,°C)
$La_{0.7}Sr_{0.3}Fe_{0.9}Ni_{0.1}O_3$	119.0	173.7	210.6	234.6	252.6	255.5	257.2 (750)
$La_{0.7}Sr_{0.3}Fe_{0.8}Ni_{0.2}O_3$	423.1	492.4	538.7	569.4	519.4	601.4	601.4 (800)
$La_{0.7}Sr_{0.3}Fe_{0.7}Ni_{0.3}O_3$	485.9	552.3	593.3	625.7	649.9	637.1	650.5 (750)

The data revealed that the electrical conductivity increase with temperature within the region between room temperature to 800°C in air. The conductivity values increase with the increase of Ni content in the sample. It is noticed that the conductivity of 30% Ni–doped material decreased slightly from 750–800°C. Moreover, the electronic conductivity at 750°C of $La_{0.7}Sr_{0.3}Fe_{0.7}Ni_{0.3}O_3$ (650.5 S/cm) is about 3.8 times higher than that of undoped $La_{0.7}Sr_{0.3}FeO_3$ (170 S/cm). It is possible that the high electronic conductivity of $La_{0.7}Sr_{0.3}Fe_{1-x}Ni_xO_3$ might be related to the 3d orbital of the ions at the B–sites. The charge compensation for the introduction of strontium at the A–sites may cause the charge change from Fe^{3+} to Fe^{4+} and/or Ni^{2+} to Ni^{3+}. In this case, the concentration of electronic holes increase, thus increasing *p*–type conductivity. The conductivity of $La_{0.7}Sr_{0.3}Fe_{1-x}Ni_xO_3$ in this work is greater than that of $La_{0.7}Sr_{0.3}Cr_{0.95}Ni_{0.05}O_{3-\delta}$ anode (3 S/cm in air at 900°C) reported by Irvine [35]. Therefore, the higher conductivity of $La_{0.7}Sr_{0.3}Fe_{0.7}Ni_{0.3}O_3$ might rise from the enhancement of nickel ions in the lattice. The cell volume of $La_{0.7}Sr_{0.3}Fe_{0.7}Ni_{0.3}O_3$ in air is 58.1 $Å^3$ which is smaller than that of $La_{0.7}Sr_{0.3}Cr_{0.95}Ni_{0.05}O_{3-\delta}$ (232.80 $Å^3$). The small lattice means shorter A–O and B–O bonds which would facilitate charge transfer through the M–O bonds if multivalent lanthanide such as lanthanum is involved. On the other hand, short M–O bond also implies higher binding energy which may hinder the charge transfer as well [36].

The activation energies of Ni specimens were calculated from the linear part of Arrhenius plots (Figure 3.20). From Table 3.12, it can be clearly seen

that the activation energy of Ni specimens decreased with the increase of the Ni contents.

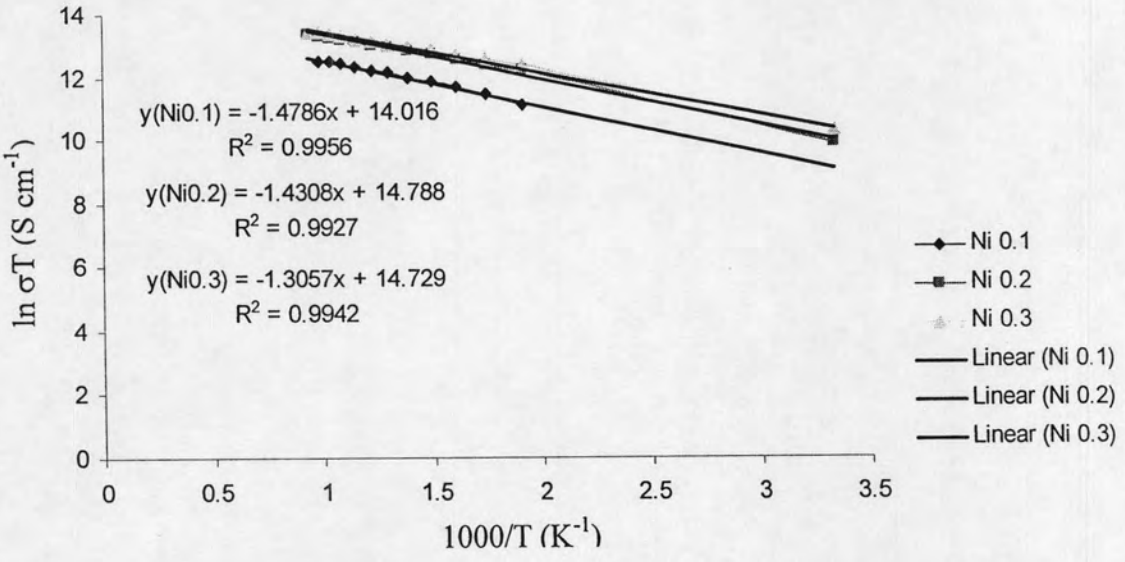

Figure 3.20 Arrhenius plot of the electrical conductivity of $La_{0.7}Sr_{0.3}Fe_{1-x}Ni_xO_3$ (x=0.1, 0.2 and 0.3).

Table 3.12 Activation energy of $La_{0.7}Sr_{0.3}FeO_3$ and $La_{0.7}Sr_{0.3}Fe_{1-x}Ni_xO_3$ (x=0.1, 0.2 and 0.3).

Sample	E_a (kJ/mol)
$La_{0.7}Sr_{0.3}FeO_3$	14.68
$La_{0.7}Sr_{0.3}Fe_{0.9}Ni_{0.1}O_3$	14.38
$La_{0.7}Sr_{0.3}Fe_{0.8}Ni_{0.2}O_3$	11.90
$La_{0.7}Sr_{0.3}Fe_{0.7}Ni_{0.3}O_3$	10.86

3.3.4.4 Electrical conductivity of $La_{0.7}Sr_{0.3}Fe_{1-x}Al_xO_3$ (x=0.1, 0.2, 0.3 and 0.4)

The temperature dependence of the electrical conductivities of the $La_{0.7}Sr_{0.3}Fe_{1-x}Al_xO_3$ (x=0.1, 0.2, 0.3 and 0.4) samples are shown in Figure 3.21 and Table 3.13.

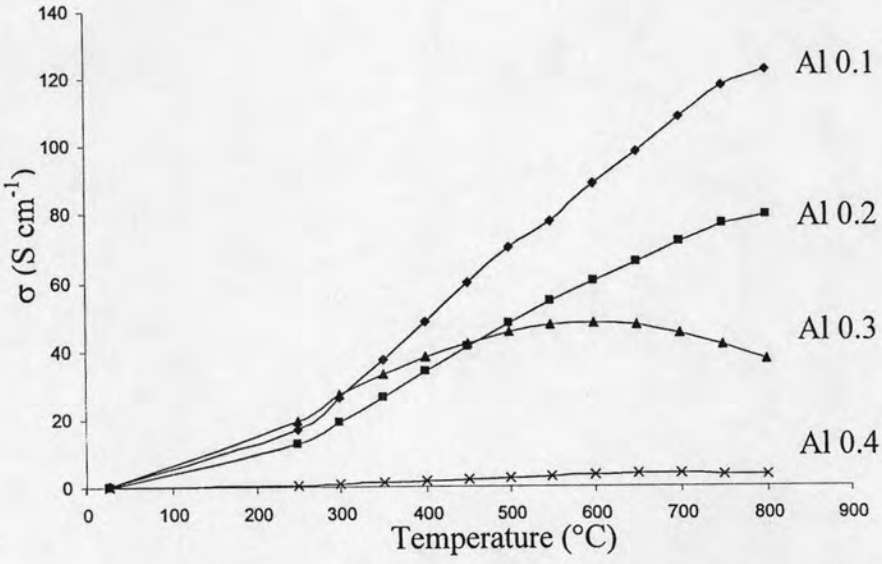

Figure 3.21 Temperature dependence of the electrical conductivity (σ) for $La_{0.7}Sr_{0.3}Fe_{1-x}Al_xO_3$ (x=0.1, 0.2, 0.3 and 0.4).

Table 3.13 Specific conductivity of $La_{0.7}Sr_{0.3}Fe_{1-x}Al_xO_3$ (x=0.1, 0.2, 0.3 and 0.4).

Sample	Specific conductivity, σ (S/cm)						
	300°C	400°C	500°C	600°C	700°C	800°C	σ_{max} (T,°C)
$La_{0.7}Sr_{0.3}Fe_{0.9}Al_{0.1}O_3$	26.4	48.5	70.0	88.7	108.2	122.3	122.3 (800)
$La_{0.7}Sr_{0.3}Fe_{0.8}Al_{0.2}O_3$	19.2	33.8	47.9	60.1	71.8	79.4	79.4 (800)
$La_{0.7}Sr_{0.3}Fe_{0.7}Al_{0.3}O_3$	27.2	38.0	45.2	48.1	45.1	37.4	48.1 (600)
$La_{0.7}Sr_{0.3}Fe_{0.6}Al_{0.4}O_3$	0.89	1.63	2.56	3.48	3.72	3.38	3.72 (700)

From Figure 3.21 and Table 3.13, the conductivity of $La_{0.7}Sr_{0.3}Fe_{0.9}Al_{0.1}O_3$ reaches the maximum value of 122.3 S cm^{-1} at about 800°C. In comparison of the conductivities various Al–doped specimens, the conductivity decreases with an increase of Al content. The decrease in conductivity of $La_{0.7}Sr_{0.3}Fe_{1-x}Al_xO_3$ is largely due to two main reasons. Firstly, aluminum doping decreases the material density and the number of pores increase with an increasing content of aluminum, resulting in the decrease of the electron mobility. The second reason can be ascribed to the fact that aluminum fixedly holds trivalent state, which can not contribute to the conductivity. With aluminum doping in B–sites, the conductivity will decrease as expected, due to the decrease of the total concentration of B–sites that participate in the electronic transport process.

The activation energy of $La_{0.7}Sr_{0.3}Fe_{1-x}Al_xO_3$ (x=0.1, 0.2, 0.3 and 0.4) specimens calculated from the linear part of Figure 3.22 are shown in Table 3.14. The activation energy of $La_{0.7}Sr_{0.3}Fe_{1-x}Al_xO_3$ is higher than that of $La_{0.7}Sr_{0.3}FeO_3$ and the activation energy increases with the amount of aluminum.

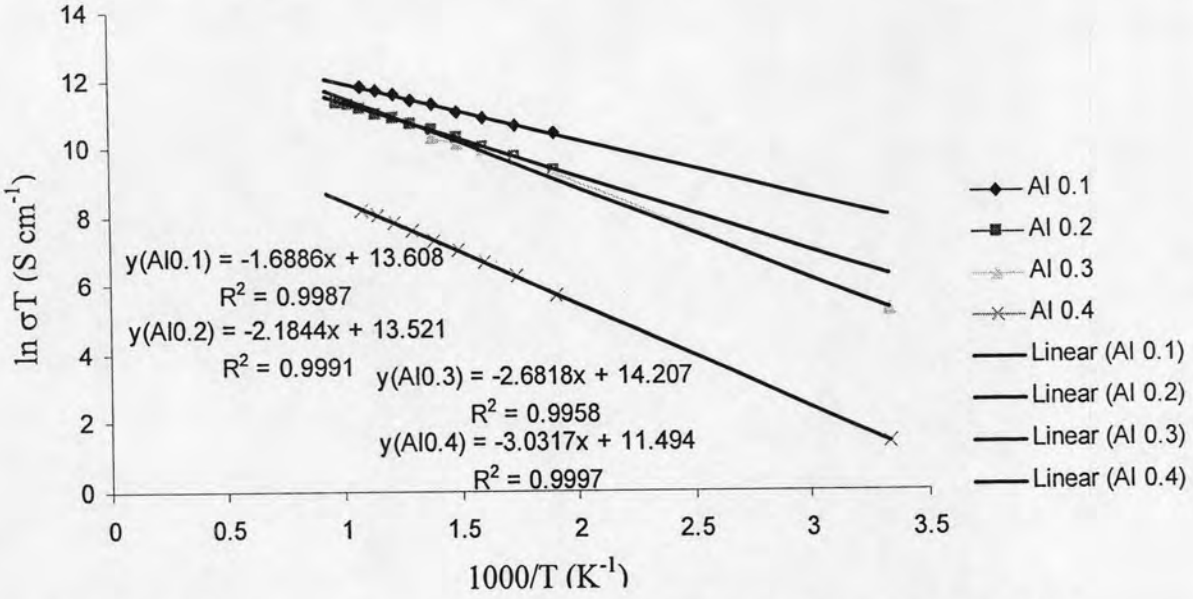

Figure 3.22 Arrhenius plot of the electrical conductivity of $La_{0.7}Sr_{0.3}Fe_{1-x}Al_xO_3$ (x=0.1, 0.2, 0.3 and 0.4).

Table 3.14 Activation energy of $La_{0.7}Sr_{0.3}FeO_3$ and $La_{0.7}Sr_{0.3}Fe_{1-x}Al_xO_3$ (x=0.1, 0.2, 0.3 and 0.4).

Sample	E_a (kJ/mol)
$La_{0.7}Sr_{0.3}FeO_3$	14.68
$La_{0.7}Sr_{0.3}Fe_{0.9}Al_{0.1}O_3$	21.32
$La_{0.7}Sr_{0.3}Fe_{0.8}Al_{0.2}O_3$	21.46
$La_{0.7}Sr_{0.3}Fe_{0.7}Al_{0.3}O_3$	22.30
$La_{0.7}Sr_{0.3}Fe_{0.6}Al_{0.4}O_3$	25.21

3.3.4.5 Electrical conductivity of $La_{0.7}Sr_{0.3}Fe_{1-x}Mn_xO_3$ (x=0.1 and 0.2)

The temperature dependence of the electrical conductivities of the $La_{0.7}Sr_{0.3}Fe_{1-x}Mn_xO_3$ (x=0.1 and 0.2) samples are shown in Figure 3.23 and Table 3.15.

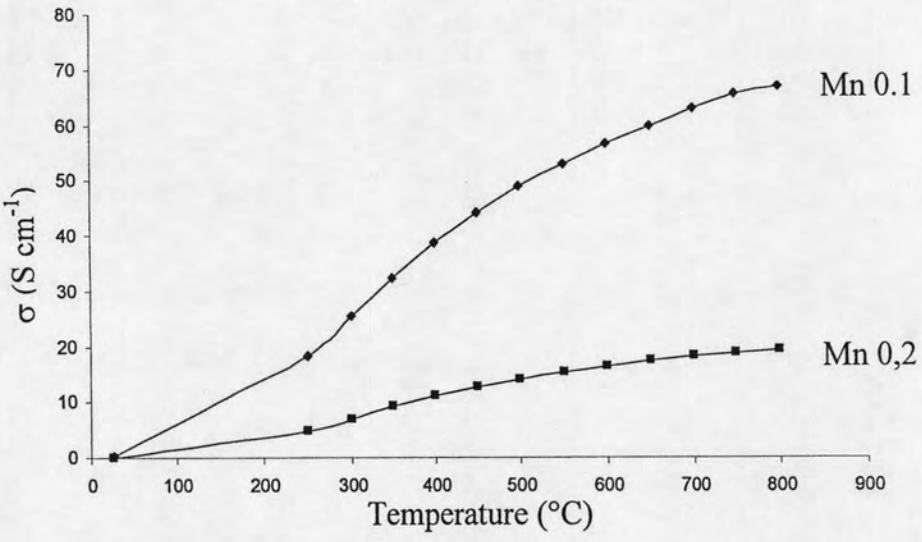

Figure 3.23 Temperature dependence of the electrical conductivity (σ) for $La_{0.7}Sr_{0.3}Fe_{1-x}Mn_xO_3$ (x=0.1 and 0.2).

Table 3.15 Specific conductivity of $La_{0.7}Sr_{0.3}Fe_{1-x}Mn_xO_3$ (x=0.1 and 0.2).

Sample	Specific conductivity, σ (S/cm)						
	300°C	400°C	500°C	600°C	700°C	800°C	σ_{max} (T,°C)
$La_{0.7}Sr_{0.3}Fe_{0.9}Mn_{0.1}O_3$	25.5	38.7	48.9	56.7	63.1	66.9	66.9 (800)
$La_{0.7}Sr_{0.3}Fe_{0.8}Mn_{0.2}O_3$	7.00	11.1	14.1	16.5	18.2	19.3	19.3 (800)

Figure 3.23 shows the result of Mn doping at B–site of $La_{0.7}Sr_{0.3}FeO_3$. Mn–doped materials exhibit lower electrical conductivity than $La_{0.7}Sr_{0.3}FeO_3$ and their conductivity increases with temperature (semi–conductor type). The maximum electrical conductivity of $La_{0.7}Sr_{0.3}Fe_{0.9}Mn_{0.1}O_3$ (66.9 S/cm at 800°C) is higher than that of $La_{0.7}Sr_{0.3}Fe_{0.8}Mn_{0.2}O_3$, suggesting the higher density of the former. However, the conductivity value of 10% Mn-doped oxide is greater than $(La_{0.75}Sr_{0.25})_{0.95}Cr_{0.5}Mn_{0.5}O_{3-\delta}$ (20–35 S/cm) reported by Kharton [37].

The activation energy of $La_{0.7}Sr_{0.3}Fe_{1-x}Mn_xO_3$ (x=0.1 and 0.2) specimens calculated from the linear part of Figure 3.24 are listed in Table 3.16. The activation energy of $La_{0.7}Sr_{0.3}Fe_{1-x}Mn_xO_3$ (x=0.1 and 0.2) are higher than that of $La_{0.7}Sr_{0.3}FeO_3$. It can be clearly seen that the activation energy of Mn specimens increases with the Mn content.

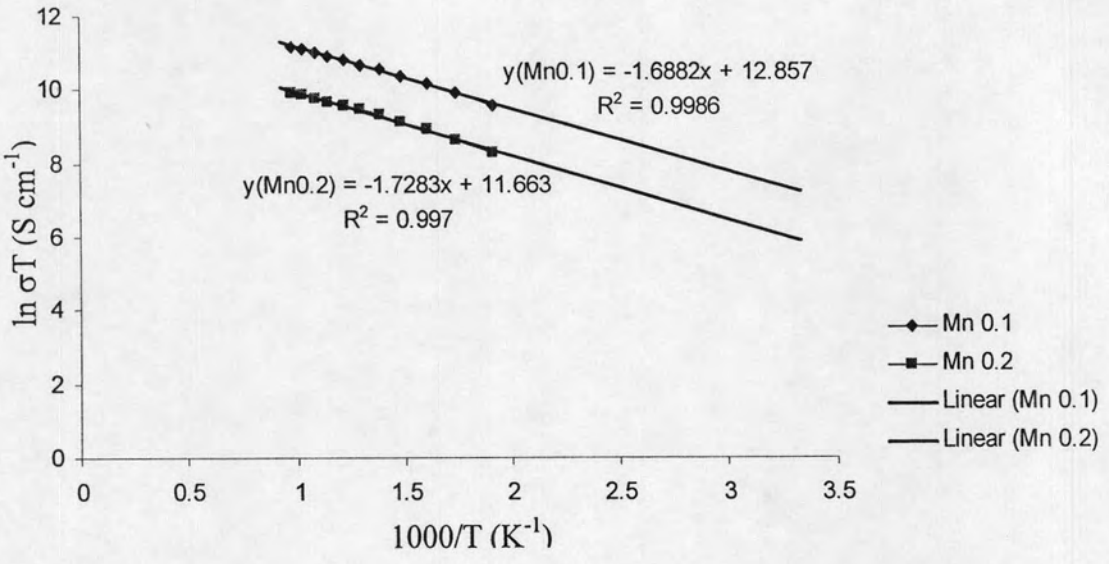

Figure 3.24 Arrhenius plot of the electrical conductivity of $La_{0.7}Sr_{0.3}Fe_{1-x}Mn_xO_3$ (x=0.1 and 0.2).

Table 3.16 Activation energy of $La_{0.7}Sr_{0.3}FeO_3$ and $La_{0.7}Sr_{0.3}Fe_{1-x}Mn_xO_3$ (x=0.1 and 0.2).

Sample	E_a (kJ/mol)
$La_{0.7}Sr_{0.3}FeO_3$	14.68
$La_{0.7}Sr_{0.3}Fe_{0.9}Mn_{0.1}O_3$	16.78
$La_{0.7}Sr_{0.3}Fe_{0.8}Mn_{0.2}O_3$	17.54

From the conductivity part, it can be seen that doping with Cu and Ni at B–site can improve the conductivity of $La_{0.7}Sr_{0.3}FeO_3$. However, another important property of material for using as anode in solid oxide fuel cell is thermal expansion. The thermal expansion coefficients of Cu and Ni–doped oxides were measured by dilatometer.

3.3.5 The thermal expansion coefficients

Since SOFCs operate at high temperatures and should endure the thermal cycle from room temperature to operating temperature, anode must be thermally compatible with the other cell components. Therefore, the thermal expansion coefficient (TEC) of SOFC anode must be close to those of the other cell components to minimize the thermal stresses.

3.3.5.1 The thermal expansion coefficients of $La_{0.7}Sr_{0.3}FeO_3$

Figure 3.25 illustrates the thermal expansion of $La_{0.7}Sr_{0.3}FeO_3$ measured in air and the temperature range from room temperature to 800°C

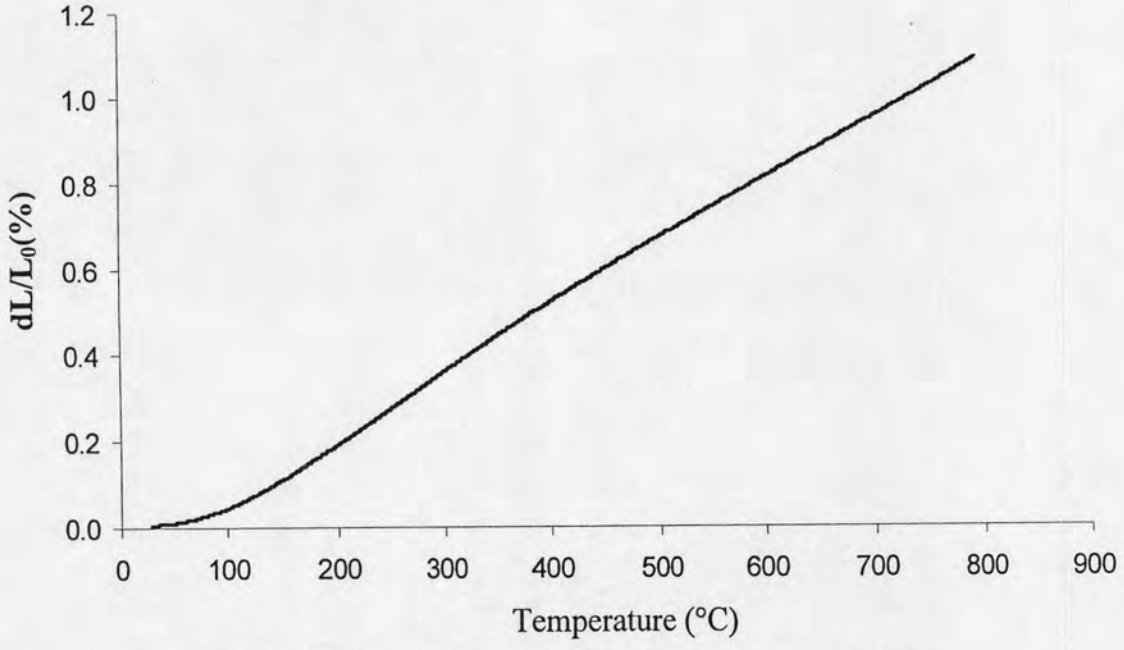

Figure 3.25 The thermal expansion curves for $La_{0.7}Sr_{0.3}FeO_3$.

The perovskite oxides expanded almost linearly in the measured temperature. The lattice expansion observed may be attributed to the loss of oxygen and the formation of oxygen vacancies. There were two reasons for the lattice expansion concerned with the formation of oxygen vacancies. Firstly, the repulsion force arising between those mutually exposed cations when oxygen ions are extracted from the lattice. Secondly, the increase in cation size due to the reduction of Fe ions from higher to lower valences, which must occur concurrently with formation of oxygen vacancies in order to maintain electrical neutrality, described in equation (1) [42-44].

$$2Fe_{Fe}^{\bullet} + O_O^{x} \rightleftharpoons 2Fe_{Fe}^{x} + V_O^{\bullet\bullet} + \frac{1}{2}O_2 \quad (1)$$

Thermal reduction of Fe^{4+} to Fe^{3+} was found to occur at about 370°C. The thermal expansion curves occurred turning around this temperature suggested the reduction of Fe^{4+}. Therefore, the formation of oxygen vacancies enhanced the thermal expansion coefficients.

The linear thermal expansion coefficient obtained from the slopes of the thermal expansion curves of Figure 3.25. The thermal expansion of $La_{0.7}Sr_{0.3}FeO_3$ at 100–700°C measured in this work is lower as compared to other ferrite perovskite, such as $La_{0.6}Sr_{0.4}FeO_3$, $La_{0.7}Sr_{0.3}FeO_3$ and $La_{0.8}Sr_{0.2}FeO_3$ (Table 3.17).

Table 3.17 The TEC values of $La_{1-x}Sr_xFeO_3$ (x= 0.2, 0.3 and 0.4).

sample	TEC (x $10^{-6}K^{-1}$)	reference
$La_{0.6}Sr_{0.4}FeO_3$	16.3	[38]
$La_{0.7}Sr_{0.3}FeO_3$	16.3	[39]
$La_{0.7}Sr_{0.3}FeO_3$	15.2	This work
$La_{0.8}Sr_{0.2}FeO_3$	15.8	[40]

From Table 3.17, it can be clearly seen that TEC of $La_{0.7}Sr_{0.3}FeO_3$ obtained this work is less than previous work revealed by Ullmann *et al.* [39]. This sample was synthesized from the same sol-gel citrate method as presented in this work but using different conditions.

3.3.5.2 The thermal expansion coefficients of $La_{0.7}Sr_{0.3}Fe_{1-x}Cu_xO_3$ (x=0.1 and 0.2).

The thermal expansion curves are shown in Figure 3.26 and TEC of the oxides are listed in Table 3.18. As compared to $La_{0.7}Sr_{0.3}FeO_3$ the thermal expansion coefficient of $La_{0.7}Sr_{0.3}Fe_{0.9}Cu_{0.1}O_3$ and $La_{0.7}Sr_{0.3}Fe_{0.8}Cu_{0.2}O_3$ does not change significantly.

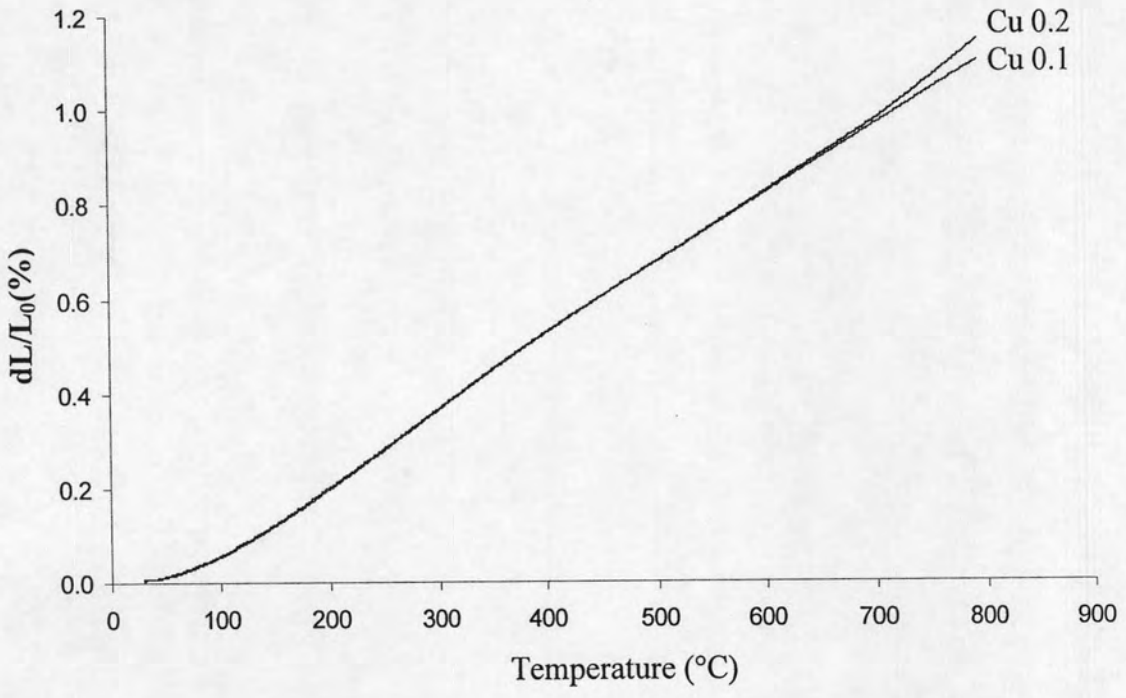

Figure 3.26 The thermal expansion curves for $La_{0.7}Sr_{0.3}Fe_{1-x}Cu_xO_3$ (x=0.1 and 0.2).

Table 3.18 The TEC values of $La_{0.7}Sr_{0.3}Fe_{1-x}Cu_xO_3$ (x=0, 0.1 and 0.2).

sample	TEC (x $10^{-6}K^{-1}$)
$La_{0.7}Sr_{0.3}FeO_3$	15.2
$La_{0.7}Sr_{0.3}Fe_{0.9}Cu_{0.1}O_3$	15.2
$La_{0.7}Sr_{0.3}Fe_{0.8}Cu_{0.2}O_3$	15.3

3.3.5.3 The thermal expansion coefficients of $La_{0.7}Sr_{0.3}Fe_{1-x}Ni_xO_3$ (x=0.1, 0.2 and 0.3).

The thermal expansion curves are shown in Figure 3.27 and TEC of the oxides are listed in Table 3.19. The thermal expansion coefficient of Ni^{2+} samples increased with increasing the amount of Ni^{2+} corresponding to the works of Kharton, *et al.* [41] explained that the average thermal expansion coefficients of $La_{1-y}Sr_yFe_{1-x}Ni_xO_{3-\delta}$ (x=0.1–0.4, y=0.1–0.2) ceramics rising with strontium and nickel contents. Its value vary in the ranges (12.4–13.4) × $10^{-6}K^{-1}$ at 700–1150K and (14.2–18.0) × $10^{-6}K^{-1}$ at 1150–1370K.

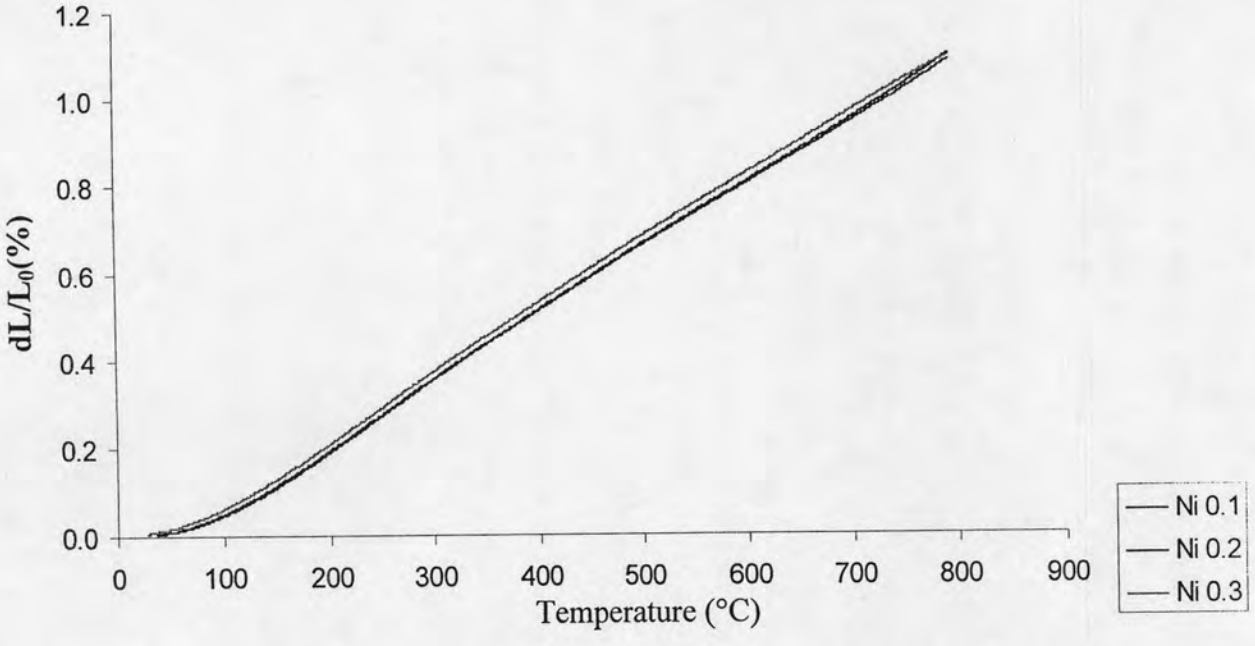

Figure 3.27 The thermal expansion curves for $La_{0.7}Sr_{0.3}Fe_{1-x}Ni_xO_3$ (x=0.1, 0.2 and 0.3).

Table 3.19 The TEC values of $La_{0.7}Sr_{0.3}Fe_{1-x}Ni_xO_3$ (x=0, 0.1, 0.2 and 0.3).

sample	TEC (x $10^{-6}K^{-1}$)
$La_{0.7}Sr_{0.3}FeO_3$	15.2
$La_{0.7}Sr_{0.3}Fe_{0.9}Ni_{0.1}O_3$	14.9
$La_{0.7}Sr_{0.3}Fe_{0.8}Ni_{0.2}O_3$	15.0
$La_{0.7}Sr_{0.3}Fe_{0.7}Ni_{0.3}O_3$	15.1

Increasing temperature leads to progressive oxygen losses from $La_{0.7}Sr_{0.3}Fe_{1-x}Ni_xO_3$ lattice and to decreasing oxidation states of the transition metal. As expected, this effect becomes more pronounced with strontium and nickel additions. The resultant chemical contribution to the lattice expansion cause the thermal expansion coefficient of Ni^{2+} samples increased with increasing the amount of Ni^{2+}[41].

This work shows the TEC of the prepared perovskite are very close, both at low and high temperatures (room temperature to 800°C), demonstrate that no phase change when temperature increases.